INTERNATIONAL JOURNAL FOR NUMERICAL METHODS IN FLUIDS
Int. J. Numer. Meth. Fluids 2005; **47**:619–631
Published online 17 December 2004 in Wiley InterScience (www.interscience.wiley.com). DOI: 10.1002/fld.835

Fluid–structure interaction modelling of parachute soft-landing dynamics

Keith Stein[1,*,†], Tayfun E. Tezduyar[2], Sunil Sathe[2], Richard Benney[3] and Richard Charles[3]

[1]*Department of Physics, Bethel University, St. Paul, MN, 55112, U.S.A.*
[2]*Mechanical Engineering, Rice University, MS 321, 6100 Main Street, Houston, TX 77005, U.S.A.*
[3]*U.S. Army Natick Soldier Center, Kansas Street, Natick, MA, 10760, U.S.A.*

SUMMARY

Soft landing of a payload with the aid of a retraction device is an important aspect in cargo parachute operations. Accurate simulation of this class of parachute operations with a computer model that takes into account the fluid–structure interactions involved would complement drop tests and support the design of cargo parachute systems. We describe the computational methods developed for this purpose, demonstrate how the computational model works in investigation of different soft-landing conditions, and show a good correlation between the data from our simulations and drop tests. Copyright © 2004 John Wiley & Sons, Ltd.

KEY WORDS: flow simulation; parachute aerodynamics; soft landing; fluid–structure interactions

1. INTRODUCTION

For many airdrop applications, payloads must be delivered at sufficiently high descent speeds to reduce vulnerability from enemy fire and to minimize drop-zone dispersion. Yet the landing has to be soft enough to prevent harm to the payload. These requirements motivate the development of parachute retraction systems, which provide one solution to soft-landing requirements. In these systems, a retraction device, such as a pneumatic muscle or mechanical retractor actuator, is placed between the parachute suspension lines and the payload. This causes a rapid contraction at landing, resulting in reduced impact. During and immediately after retraction the performance of a parachute is strongly influenced by fluid–structure interactions that play an important role in parachute systems dynamics. In this paper, we describe

*Correspondence to: Keith Stein, Department of Physics, Bethel University, St. Paul, MN, 55112, U.S.A.
†E-mail: k-stein@bethel.edu

Contract/grant sponsor: Army Natick Soldier Center
Contract/grant sponsor: NASA JSC

Received 20 October 2003
Accepted 18 August 2004

our parachute fluid–structure interaction modelling techniques and the special considerations for parachute soft-landing applications. Our simulations focus on soft-landing fluid–structure interactions of a single, round parachute. The retraction is represented by a set of control-line inputs, which are accounted for within the structural dynamics part of our coupled fluid–structure interaction model.

These simulations, in addition to providing preliminary results for a class of parachute fluid–structure interactions, show how the computational methods described can be used for parachute applications in general. The interaction between the parachute canopy and the surrounding flow field is an essential component of a realistic parachute simulation, and thus the ability to predict parachute fluid–structure interactions is recognized as an important challenge within the parachute research community [1, 2]. Our computational methods have been developed to address a variety of challenges in the modelling of parachute fluid–structure interactions and other fluid–structure interactions involving large displacements [3, 4]. These methods have been tested on a number of parachute applications, including descent characteristics of single, round parachutes [3, 4], cross parachutes [5], interactions between parachute canopies [6], and the response of round parachutes to control-line inputs [7]. Future studies will continue to focus on the fluid–structure interactions involved at various stages of parachute systems, from initial deployment to landing and for single and clustered parachute systems.

For all simulations described in this paper, the parachutes are operating at sufficiently low speeds, and, therefore, the aerodynamics is governed by the Navier–Stokes equations of incompressible flows. In fluid–structure interactions, because the canopies undergo shape changes, the spatial domain occupied by the fluid is varying (i.e. deforming) with respect to time. Therefore we use the deforming-spatial-domain/stabilized space–time (DSD/SST) formulation [8], which was developed for flow problems with moving boundaries and interfaces. The parachute is represented as a structure consisting of membranes, cables, and concentrated masses. The membranes and cables experience large displacements and rotation, but relatively small strains. Hence, we use a total Lagrangian formulation for the structure, with linear constitutive relationships for the membranes and cables [9].

We describe the computational model in Section 2. In Section 2.1, we provide the governing equations for the fluid dynamics and describe the DSD/SST formulation. In Section 2.2, we provide the governing equations for the cable–membrane structural dynamics and describe the finite element formulation used. In Section 2.3, we describe our mesh update methods that handle the mesh as the spatial domain occupied by the fluid changes its shape while the structure moves and deforms. Simulations for soft-landing retractions of a round parachute under a number of landing conditions are presented in Section 3. In Section 3.1, we investigate the influence of different retraction rates on soft-landing behaviour of a T–10 parachute. In Section 3.2, we compare, for soft landing of a T–10 parachute, data from our simulations to available data from drop tests. Concluding remarks are provided in Section 4.

2. COMPUTATIONAL MODEL

The computational model consists of three parts: a fluid dynamics solver, a structural dynamics solver, and a linear elasticity solver for automatic mesh moving. In our current implementation the fluid–structure coupling is achieved with an iterative technique. In this technique, the

exchange of fluid force and structural displacement data between the fluid and structure takes place within the non-linear iteration loop of each time step. Multiple non-linear iterations are carried out to improve the convergence of the coupled system. Implicit time-integration methods are used for both the fluid and structural parts. For cases where non-matching meshes are used to represent the fluid and structure at the interface, the fluid force and displacement data is exchanged by using least-squares projection.

2.1. Fluid dynamics

Let $\Omega_t \subset \mathbb{R}^{n_{sd}}$ be the spatial fluid mechanics domain with boundary Γ_t at time $t \in (0, T)$, where the subscript t indicates the time-dependence of the spatial domain and its boundary. The Navier–Stokes equations of incompressible flows can be written on Ω_t and $\forall t \in (0, T)$ as

$$\rho\left(\frac{\partial \mathbf{u}}{\partial t} + \mathbf{u}\cdot\nabla\mathbf{u} - \mathbf{f}\right) - \nabla\cdot\boldsymbol{\sigma} = 0 \tag{1}$$

$$\nabla\cdot\mathbf{u} = 0 \tag{2}$$

where ρ, $\mathbf{u}$ and $\mathbf{f}$ are the density, velocity and the external force, respectively. The stress tensor $\boldsymbol{\sigma}$ is defined as

$$\boldsymbol{\sigma}(p, \mathbf{u}) = -p\mathbf{I} + 2\mu\boldsymbol{\varepsilon}(\mathbf{u}) \tag{3}$$

Here p, $\mathbf{I}$ and μ are the pressure, identity tensor and the viscosity, respectively. The strain rate tensor is defined as

$$\boldsymbol{\varepsilon}(\mathbf{u}) = \frac{1}{2}((\nabla\mathbf{u}) + (\nabla\mathbf{u})^{\mathrm{T}}) \tag{4}$$

Both Dirichlet- and Neumann-type boundary conditions are accounted for

$$\mathbf{u} = \mathbf{g} \text{ on } (\Gamma_t)_g, \quad \mathbf{n}\cdot\boldsymbol{\sigma} = \mathbf{h} \text{ on } (\Gamma_t)_h \tag{5}$$

Here $(\Gamma_t)_g$ and $(\Gamma_t)_h$ are complementary subsets of the boundary Γ_t, $\mathbf{n}$ is the unit normal vector at the boundary, and $\mathbf{g}$ and $\mathbf{h}$ are given functions. A divergence-free velocity field is specified as the initial condition.

In the DSD/SST method the finite element formulation of the governing equations is written over a sequence of N space–time slabs Q_n, where Q_n is the slice of the space–time domain between the time levels t_n and t_{n+1}. At each time step, the integrations involved in the finite element formulation are performed over Q_n. The space–time finite element interpolation functions are continuous within a space–time slab, but discontinuous from one space–time slab to another. The notation $(\cdot)_n^-$ and $(\cdot)_n^+$ denotes the function values at t_n as approached from below and above. Each Q_n is decomposed into space–time elements Q_n^e, where $e = 1, 2, \ldots, (n_{\mathrm{el}})_n$. The subscript n used with n_{el} is to account for the general case in which the number of space–time elements may change from one space–time slab to another. The Dirichlet- and Neumann-type boundary conditions are enforced over $(P_n)_g$ and $(P_n)_h$, the complementary subsets of the lateral boundary of the space–time slab. The finite element trial function spaces $(\mathscr{S}_{\mathbf{u}}^h)_n$ for velocity and $(\mathscr{S}_p^h)_n$ for pressure, and the test function spaces $(\mathscr{V}_{\mathbf{u}}^h)_n$ and $(\mathscr{V}_p^h)_n = (\mathscr{S}_p^h)_n$ are defined by using, over Q_n, first-order polynomials in both space

and time. The DSD/SST formulation is written as follows: given $(\mathbf{u}^h)_n^-$, find $\mathbf{u}^h \in (\mathscr{S}_{\mathbf{u}}^h)_n$ and $p^h \in (\mathscr{S}_p^h)_n$ such that $\forall \mathbf{w}^h \in (\mathscr{V}_{\mathbf{u}}^h)_n$ and $q^h \in (\mathscr{V}_p^h)_n$:

$$\begin{aligned}
&\int_{Q_n} \mathbf{w}^h \cdot \rho \left(\frac{\partial \mathbf{u}^h}{\partial t} + \mathbf{u}^h \cdot \nabla \mathbf{u}^h - \mathbf{f}^h \right) \mathrm{d}Q + \int_{Q_n} \boldsymbol{\varepsilon}(\mathbf{w}^h) : \boldsymbol{\sigma}(p^h, \mathbf{u}^h)\, \mathrm{d}Q \\
&\quad - \int_{(P_n)_h} \mathbf{w}^h \cdot \mathbf{h}^h \, \mathrm{d}P + \int_{Q_n} q^h \nabla \cdot \mathbf{u}^h \, \mathrm{d}Q + \int_{\Omega_n} (\mathbf{w}^h)_n^+ \cdot \rho((\mathbf{u}^h)_n^+ - (\mathbf{u}^h)_n^-)\, \mathrm{d}\Omega \\
&\quad + \sum_{e=1}^{(n_{\mathrm{el}})_n} \int_{Q_n^e} \frac{1}{\rho} \left[\tau_{\mathrm{SUPG}} \rho \left(\frac{\partial \mathbf{w}^h}{\partial t} + \mathbf{u}^h \cdot \nabla \mathbf{w}^h \right) + \tau_{\mathrm{PSPG}} \nabla q^h \right] \cdot \\
&\qquad \left[\rho \left(\frac{\partial \mathbf{u}^h}{\partial t} + \mathbf{u}^h \cdot \nabla \mathbf{u}^h \right) - \nabla \cdot \boldsymbol{\sigma}(p^h, \mathbf{u}^h) - \rho \mathbf{f}^h \right] \mathrm{d}Q \\
&\quad + \sum_{e=1}^{n_{\mathrm{el}}} \int_{Q_n^e} \nu_{\mathrm{LSIC}} \nabla \cdot \mathbf{w}^h \rho \nabla \cdot \mathbf{u}^h \, \mathrm{d}Q = 0
\end{aligned} \tag{6}$$

where τ_{SUPG} (streamline-upwind/Petrov–Galerkin), τ_{PSPG} (pressure-stabilizing/Petrov–Galerkin), and ν_{LSIC} (least-squares on incompressibility constraint) are the stabilization parameters (see Reference [10]). This formulation is applied to all space–time slabs $Q_0, Q_1, Q_2, \ldots, Q_{N-1}$, starting with $(\mathbf{u}^h)_0^- = \mathbf{u}_0$. For an earlier, detailed reference on this stabilized formulation see Reference [8]. The SUPG and PSPG formulations were introduced in References [8, 11], respectively. An earlier version of the pressure-stabilizing formulation for Stokes flows was reported in Reference [12]. The stabilized space–time formulations were used earlier by other researchers to solve problems with fixed spatial domains (see for example Reference [13]).

2.2. Structural dynamics

Let $\Omega_t^s \subset \mathbb{R}^{n_{xd}}$ be the spatial domain bounded by Γ_t^s, where $n_{xd} = 2$ for membranes and $n_{xd} = 1$ for cables. The boundary Γ_t^s is composed of $(\Gamma_t^s)_g$ and $(\Gamma_t^s)_h$. Here, the superscript 's' corresponds to the structure. The equations of motion for the structural system are:

$$\rho^s \left(\frac{\mathrm{d}^2 \mathbf{y}}{\mathrm{d}t^2} + \eta \frac{\mathrm{d}\mathbf{y}}{\mathrm{d}t} - \mathbf{f}^s \right) - \nabla \cdot \boldsymbol{\sigma}^s = \mathbf{0} \tag{7}$$

where, $\mathbf{y}$ is the displacement, ρ^s is the material density, $\mathbf{f}^s$ are the external body forces, $\boldsymbol{\sigma}^s$ is the Cauchy stress tensor, and η is the mass-proportional damping coefficient. The damping provides additional stability and may be used for problems where time-accuracy is not important.

In our numerical method, a Lagrangian formulation of the problem is used. Thus, stresses are expressed in terms of the 2nd Piola–Kirchoff stress tensor $\mathbf{S}$, which is related to the Cauchy stress tensor through a kinematic transformation. Under the assumption of large displacements and rotations, small strains, and no material damping, the membranes and cables are treated as Hookean materials with linear elastic properties. For membranes, under the assumption of

plane stress, $\mathbf{S}$ becomes

$$S^{ij} = (\bar{\lambda}_m G^{ij} G^{kl} + \mu_m [G^{il} G^{jk} + G^{ik} G^{jl}]) E_{kl} \tag{8}$$

where for the case of isotropic plane stress

$$\bar{\lambda}_m = \frac{2\lambda_m \mu_m}{(\lambda_m + 2\mu_m)} \tag{9}$$

Here, E_{kl} are the components of the Cauchy–Green strain tensor, G^{ij} are the components of the contravariant metric tensor in the original configuration, and λ_m and μ_m are Lamé constants. For cables, under the assumption of uniaxial tension, $\mathbf{S}$ becomes

$$S^{11} = E_c G^{11} G^{11} E_{11} \tag{10}$$

where E_c is the cable Young's modulus. To account for stiffness-proportional material damping, the Hookean stress–strain relationships defined by Equations (8) and (10) are modified, and E_{kl} is replaced by $\hat{E}_{kl}$, where

$$\hat{E}_{kl} = E_{kl} + \zeta \dot{E}_{kl} \tag{11}$$

Here, ζ is the stiffness proportional damping coefficient and $\dot{E}_{kl}$ is the time derivative of E_{kl}.

The semi-discrete finite element formulation for the structural dynamics is based on the principle of virtual work:

$$\int_{\Omega_0^s} \rho^s \frac{\mathrm{d}^2 \mathbf{y}^h}{\mathrm{d}t^2} \cdot \mathbf{w}^h \mathrm{d}\Omega^s + \int_{\Omega_0^s} \eta \rho^s \frac{\mathrm{d}\mathbf{y}^h}{\mathrm{d}t} \cdot \mathbf{w}^h \, \mathrm{d}\Omega^s$$

$$+ \int_{\Omega_0^s} \mathbf{S}^h : \delta \mathbf{E}(\mathbf{w}^h) \, \mathrm{d}\Omega^s = \int_{\Omega_t^s} (\mathbf{t} + \rho^s \mathbf{f}^s) \cdot \mathbf{w}^h \, \mathrm{d}\Omega^s \tag{12}$$

Here the weighting function $\mathbf{w}^h$ is also the virtual displacement. The air pressure force on the canopy surface is represented by vector $\mathbf{t}$. The pressure term is geometrically non-linear and thus increases the overall non-linearity of the formulation. The left-hand side terms of Equation (12) are referred to in the original configuration and the right-hand side terms for the deformed configuration at time t.

Upon discretization using appropriate function spaces, a non-linear system of equations is obtained at each time step. In solving that non-linear system with an iterative method, we use the following incremental form:

$$\left[\frac{\mathbf{M}}{\beta \Delta t^2} + \frac{(1-\alpha)\gamma \mathbf{C}}{\beta \Delta t} + (1-\alpha)\mathbf{K} \right] \Delta \mathbf{d}^i = \mathbf{R}^i \tag{13}$$

where

$$\mathbf{C} = \eta \mathbf{M} + \zeta \mathbf{K} \tag{14}$$

Here $\mathbf{M}$ is the mass matrix, $\mathbf{K}$ is the consistent tangent matrix associated with the internal elastic forces, $\mathbf{C}$ is a damping matrix, $\mathbf{R}^i$ is the residual vector at the ith iteration, and $\Delta \mathbf{d}^i$

is the ith increment in the nodal displacements vector $\mathbf{d}$. The damping matrix $\mathbf{C}$ is used only in stand-alone structural mechanics computations while establishing an inflated canopy shape as the starting shape for the fluid–structure interaction computations. In Equation (13), all of the terms known from the previous iteration are lumped into the residual vector $\mathbf{R}^i$. The parameters α, β, γ are part of the Hilber–Hughes–Taylor [14] scheme, which is used here for time-integration.

2.2.1. Special modelling considerations

1. *Time-dependent cable properties*: In the simulations presented in this paper, a soft-landing mechanism is represented as a single control-line input. The retraction device is modelled with a set of cables that shrink in time. This is accomplished by decreasing, over the duration of retraction, the cable reference length based on which the cable stresses are defined. The inertia terms, however, are always based on the initial reference lengths.
2. *Augmented-mass stabilization*: The iterative coupling technique used in our current implementation amounts to an approximate Newton–Raphson method, where the matrix blocks representing the coupling between the fluid and structural mechanics systems are not accounted for in the left-hand side matrix. Because of this, in fluid–structure interaction computations where the structure is light, structural response becomes very sensitive to small changes in the fluid dynamics forces and convergence becomes difficult to achieve.

   A number of approaches can be taken to deal with this difficulty. One approach is to artificially increase the inertia of the structure by increasing the first term on the left-hand side of Equation (12). This approach involves extra structural mass in the inertia terms, but not in the gravitational body force terms. We observed in our computations that, other than helping with the convergence, this has a very limited affect on the overall structural behaviour, because in the class of problems we are solving the stiffness terms are dominant compared to the inertia terms. This approach was taken in the computations presented in Section 3.2 and also in computations reported in Reference [15].

   A better approach would be the mixed method introduced in Reference [16] for the purpose of accounting for the coupling matrix blocks, including those representing the affect of mesh motion. A short cut approach for improving the convergence was introduced in References [17, 18]. In this short cut approach, it was proposed to artificially increase the structural mass contribution to the matrix block corresponding to the structural mechanics equations and unknowns to reduce 'over-correcting' (i.e. 'over-incrementing') the structural displacements during the coupling iterations. Since this is achieved without altering the right-hand-side vectors in the non-linear iterations, when the coupling iterations converge, they converge to the solution of the problem with the correct structural mass. In the context of this paper, this would be equivalent to artificially increasing the matrix $\mathbf{M}$ in Equation (13).

2.3. Mesh update method

In general the mesh update could have two components: moving the mesh for as long as it is possible, and full or partial remeshing (i.e. generating a new set of elements, and sometimes

also a new set of nodes) when the element distortion becomes too high. In mesh moving strategies, the only rule the mesh motion needs to follow is that at the moving boundary or interface the normal velocity of the mesh has to match the normal velocity of the fluid. Beyond that, the mesh can be moved in any way desired, with the main objective being to reduce the frequency of remeshing. In 3D simulations, if the remeshing requires calling an automatic mesh generator, the cost of automatic mesh generation becomes a major reason for trying to reduce the frequency of remeshing. Furthermore, when we remesh, we need to project the solution from the old mesh to the new one. This introduces projection errors. Also, in 3D, the computing time consumed by this projection step is not a trivial one. All these factors constitute a strong motivation for designing mesh update strategies that minimize the frequency of remeshing.

In parachute fluid–structure interactions problem geometries are complex and require automatic methods for mesh generation and mesh update. We use an automatic mesh moving technique, introduced in Reference [19], where motion of mesh nodes is governed by the equations of elasticity, and the mesh deformation is handled selectively based on the element sizes. As boundary condition, motion of the interface nodes is required to match the normal velocities of the fluid. With the boundary condition satisfied, motion of the internal nodes is determined by solving the equations of elasticity. Selective treatment based on element sizes is attained by altering the way the Jacobian of the transformation from the element domain to the physical domain is accounted for. The objective is to increase stiffening of the smaller elements, which are typically located near solid surfaces and, without selective treatment, can absorb excessive amounts of the mesh deformation. A more extensive type of this Jacobian-based stiffening was presented in Reference [20] by introducing a stiffening power that determines the degree by which the smaller elements are rendered stiffer than the larger ones.

3. SIMULATIONS

The T–10 is a personnel parachute constructed with a 35-ft diameter canopy and 30 suspension lines each 29.4 ft long. The suspension lines meet at a single confluence point. A 14-ft pneumatic muscle actuator (PMA) is modeled with a set of cable elements that connect the confluence point and the payload. Figure 1 shows the behaviour of a soft-landing system for a T–10 parachute and payload. The sequence of photographs were obtained from a test conducted by the US Army at Fort Benning for a soft-landing system designed by Vertigo, Inc [21]. The soft-landing retraction shown in Figure 1 is employed during the first four frames of the sequence. It is during the post-retraction stages of the soft landing that the strongest fluid–structure interactions are experienced and canopy collapse can occur. For this reason, future attention will be given to post-retraction dynamics.

3.1. Preliminary simulations: understanding the dynamics of soft-landing retraction

Successful operation of a soft-landing system requires that three conditions are met. First, forces exerted by the retraction device on the payload must not exceed some threshold that will harm the payload. Second, the payload must be decelerated to some acceptable landing velocity. Third, the payload must touch down during the ‘window of opportunity’ at which the

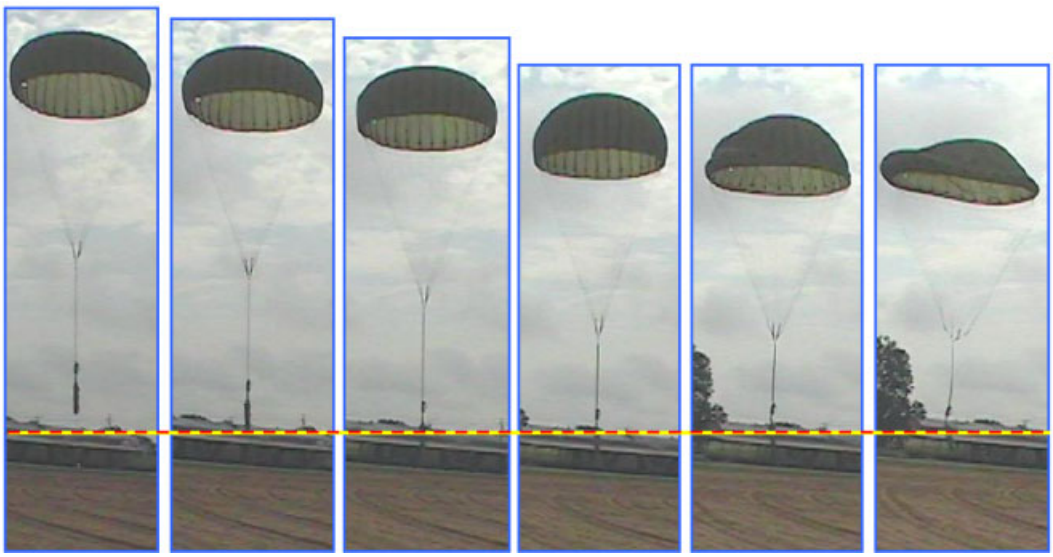

Figure 1. Parachute soft-landing sequence (photographs courtesy of US Army SBCCOM and Vertigo, Inc.).

landing velocity condition is being met. Retraction rates, in their critical role, can determine whether or not these requirements are met. Three preliminary simulations are carried out for the soft landing of a T–10 parachute system and focus on the behaviour of the system for three different retraction rates. In each case, the total parachute system weight is 300 lbf (with a payload weight of 250 lbf) and is initially descending at approximately 20 ft/s. The PMA is represented by 10 cable elements and the retraction is modelled by shrinking the cables during the soft-landing simulation. The shrinking, in the amount of 38%, is accomplished in the way described in Section 2.2, and with a constant rate of decrease during the retraction period. In each case, a computation of 400 time steps is carried out prior to initiating the soft landing. Then, shrinking of the PMA cables are prescribed to simulate the retraction durations of 0.14 s (200 time steps), 0.21 s (300 time steps), and 0.28 s (400 time steps).

The structural dynamics model is composed of membranes, cables, and a concentrated mass. The canopy is modeled with 780 biquadratic membrane elements. Linear cable elements are used to model the suspension lines, radial reinforcements along the canopy, and the PMA cables. The payload is represented by a single concentrated mass. An inflated equilibrium geometry of the parachute structure for a prescribed pressure distribution is first obtained with a stand-alone structural dynamics computation. The equilibrium canopy geometry is used as the initial condition for the fluid–structure interaction computation. The structural model for the T–10 parachute system with the PMA, the fluid mesh, and the initial flow field (pressure) are shown in Figure 2. The fluid meshes used in the computations reported here have of the order one million tetrahedral elements. From earlier parachute simulations and refinement studies [22, 23], we believe that this level of mesh refinement is sufficient to resolve the primary flow features around the parachute. Figure 3 shows, for each case, the aerodynamic drag experienced by the parachute canopy prior to, during, and immediately after

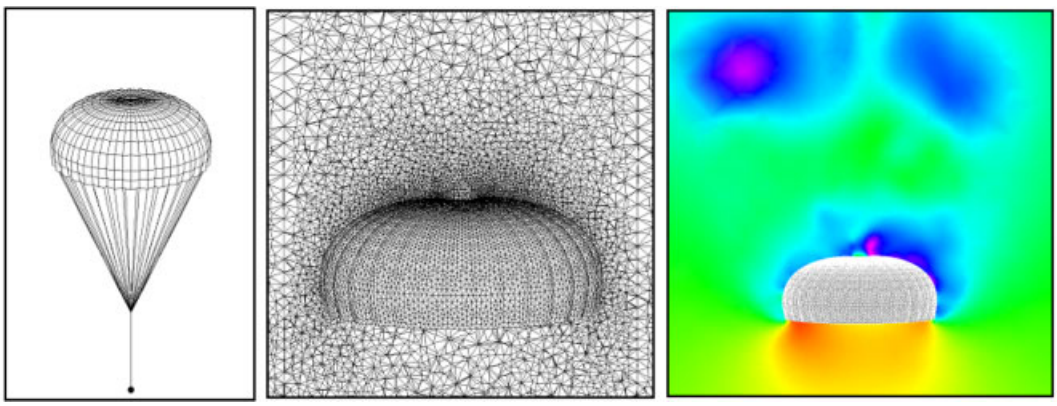

Figure 2. Structural model, fluid mesh, and initial flow field (pressure).

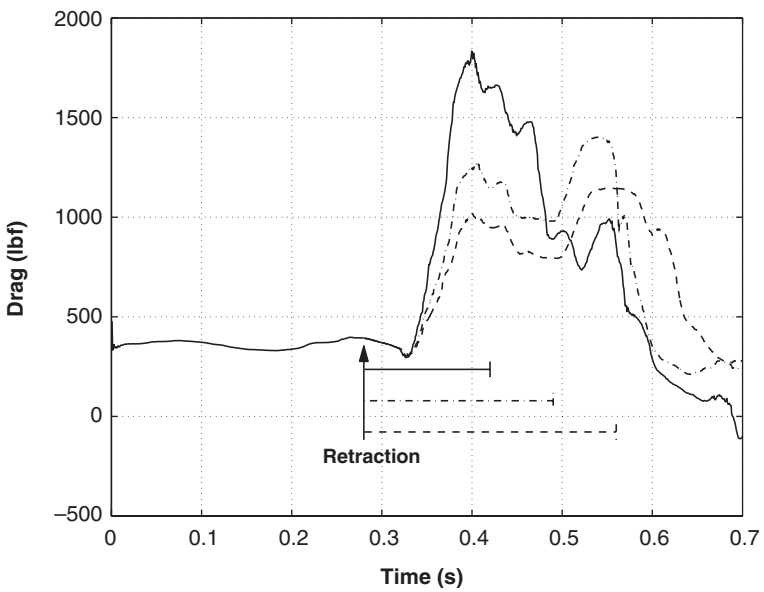

Figure 3. Soft-landing of a T–10 parachute with different retraction rates. Time-history of the drag [7].

the retraction. As expected, the curve with the largest peak drag corresponds to the fastest retraction. Figure 4 shows, for each case, the vertical positions and velocities of the payload and confluence point during the same time interval. The soft-landing behaviour is evident from the vertical velocity histories of the payload. The velocity plot indicates that minimum payload velocity is experienced shortly into the post-retraction stage of the operation. For each of the cases simulated, the retraction results in a negative velocity for the payload shortly after the retraction has been completed.

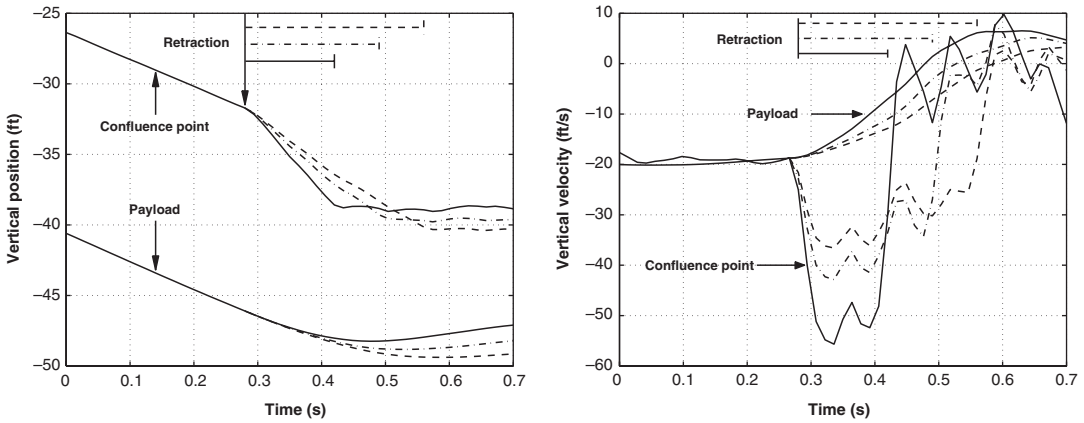

Figure 4. Soft-landing of a T–10 parachute with different retraction rates. Time-history of the position and velocity of the payload and confluence point [7].

3.2. Comparison of data from simulations and drop tests

A PMA (with mechanical valve) was drop tested from a tower at Fort Benning, under several different conditions, using a T–10 parachute. These drop tests were performed for different payloads and PMA actuation pressures. We consider two of these drop tests. Drop 7 was carried out with a 222-lbf payload and 300-psi actuation pressure. Drop 12 had a 305-lbf payload and 400-psi actuation pressure. We carried out two simulations for the purpose of comparing data from the simulations and drop tests. In both cases, the total parachute system weight is 236 lbf (with a payload weight of 222 lbf) and is initially descending at approximately 16 ft/s. Different retraction lengths are used in the two cases to simulate soft-landing behaviour that is comparable to the drop tests. Retractions are accomplished in the way described in Section 2.2, and with a constant rate of decrease during the retraction period of 0.25 s. In Simulation 1 the retraction amount is 5.3 ft (26%), and in Simulation 2 it is 4.4 ft (22%). The canopy is modelled with 5880 triangular membrane elements. The PMA is modelled with 20 cable elements.

Figure 5 shows the payload trajectory for Simulation 1, and comparison of payload velocities from the two simulations and two drop tests. There is a good, general correlation between the velocities from the simulations and drop tests. We see a closer correlation specifically between Simulation 1 and Drop 7 and between Simulation 2 and Drop 12.

4. CONCLUDING REMARKS

We described the computational methods that form the general framework of our simulation tools for parachute fluid–structure interactions. We also described how these tools can be extended specifically to simulation of the aerodynamics and fluid–structure interactions associated with the soft landing of a round parachute. We first focused on understanding the dynamics of soft-landing retraction, and investigated the influence of different retraction

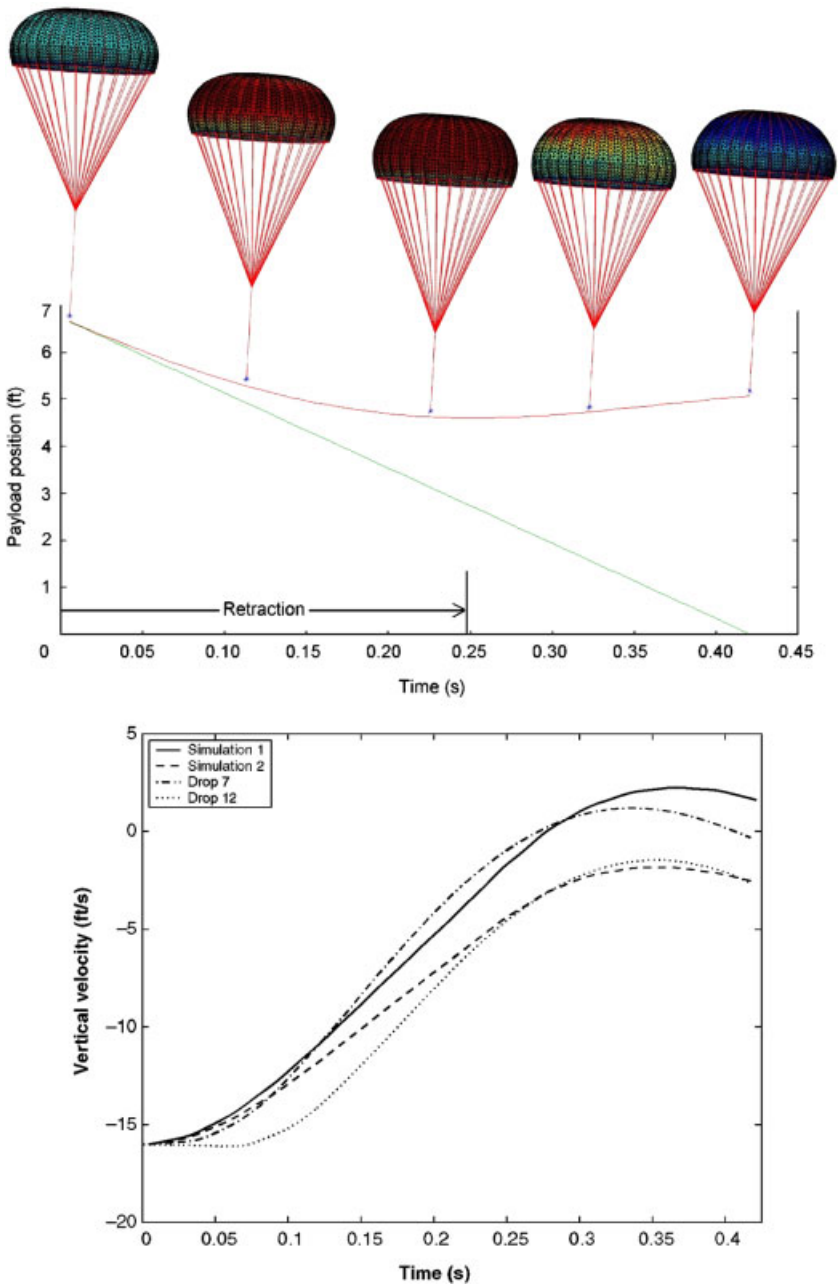

Figure 5. Comparison of data from simulations and drop tests. *Top*: Payload trajectory for Simulation 1 during and immediately after retraction. The straight line is the trajectory that the payload would have had without the retraction. The parachutes displayed illustrate the deformations of the canopy and the cables. The length scale used in displaying the parachutes is not the same as it is for the trajectory graph. *Bottom*: Payload velocity during and immediately after retraction, obtained from the two simulations and two drop tests.

rates on soft-landing performance of a T–10 parachute. We observed that for the payload the minimum velocities occur early in the post-retraction stage. We also carried out a set of simulations for the purpose of comparing, for soft landing of a T–10 parachute, data from our simulations and data from drop tests performed at Fort Benning. We observed a good correlation between the data from the simulations and drop tests.

It is evident that fluid–structure interactions play a significant role in parachute soft landing. The simulations presented in this paper demonstrate the utility of our computational models in investigation of this class of parachute applications. Future studies will include soft-landing simulations for a variety of cargo applications and more comprehensive investigation of the post-retraction dynamics of parachute soft landing.

ACKNOWLEDGEMENTS

This work was supported by the Army Natick Soldier Center and NASA JSC.

REFERENCES

1. Peterson CW, Strickland JH, Higuchi H. The fluid dynamics of parachute inflation. *Annual Review of Fluid Mechanics* 1996; **28**:361–387.
2. Benney RJ, Stein KR. A computational fluid structure interaction model for parachute inflation. *Journal of Aircraft* 1996; **33**:730–736.
3. Stein K, Benney R, Kalro V, Tezduyar TE, Leonard J, Accorsi M. Parachute fluid–structure interactions: 3-D computation. *Computer Methods in Applied Mechanics and Engineering* 2000; **190**:373–386.
4. Stein KR, Benney RJ, Tezduyar TE, Leonard JW, Accorsi M. Fluid–structure interactions of a round parachute: modelling and simulation techniques. *Journal of Aircraft* 2001; **38**:800–808.
5. Stein K, Benney R, Tezduyar T, Potvin J. Fluid–structure interactions of a cross parachute: numerical simulation. *Computer Methods in Applied Mechanics and Engineering* 2001; **191**:673–687.
6. Stein K, Tezduyar T, Kumar V, Sathe S, Benney R, Thornburg E, Kyle C, Nonoshita T. Aerodynamic interactions between parachute canopies. *Journal of Applied Mechanics* 2003; **70**:50–57.
7. Stein K, Tezduyar T, Benney R. Applications in airdrop systems: fluid–structure interaction modelling. *Proceedings of the Fifth World Congress on Computational Mechanics* (Web Site), On-line publication: http://wccm.tuwien.ac.at/, *Paper-ID: 81545*, Vienna, Austria, 2002.
8. Tezduyar TE. Stabilized finite element formulations for incompressible flow computations. *Advances in Applied Mechanics* 1991; **28**:1–44.
9. Accorsi ML, Leonard JW, Benney R, Stein K. Structural modelling of parachute dynamics. *AIAA Journal* 2000; **38**:139–146.
10. Tezduyar T, Osawa Y. Methods for parallel computation of complex flow problems. *Parallel Computing* 1999; **25**:2039–2066.
11. Hughes TJR, Brooks AN. A multi-dimensional upwind scheme with no crosswind diffusion. In *Finite Element Methods for Convection Dominated Flows*, Hughes T (ed.), AMD-Vol. 34. ASME: New York, 1979; 19–35.
12. Hughes TJR, Franca LP, Balestra M. A new finite element formulation for computational fluid dynamics: V. Circumventing the Babuška–Brezzi condition: a stable Petrov–Galerkin formulation of the Stokes problem accommodating equal-order interpolations. *Computer Methods in Applied Mechanics and Engineering* 1986; **59**:85–99.
13. Hughes TJR, Hulbert GM. Space–time finite element methods for elastodynamics: formulations and error estimates. *Computer Methods in Applied Mechanics and Engineering* 1988; **66**:339–363.
14. Hilber HM, Hughes TJR, Taylor RL. Improved numerical dissipation for time integration algorithms in structural dynamics. *Earthquake Engineering and Structural Dynamics* 1977; **5**:283–292.
15. Stein K, Tezduyar T, Sathe S, Senga M, Ozcan C, Soltys T, Kumar V, Benney R, Charles R. Simulation of parachute dynamics during control line input operations. *Proceedings of the 17th AIAA Aerodynamic Decelerator Systems Technology Conference*, *AIAA Paper 2003-2151*, Monterey, California, 2003.
16. Tezduyar TE. Finite element methods for flow problems with moving boundaries and interfaces. *Archives of Computational Methods in Engineering* 2001; **8**:83–130.
17. Tezduyar TE. Finite element methods for fluid dynamics with moving boundaries and interfaces. *Encyclopedia of Computational Mechanics*, Stein E, De Borst R, Hughes TJR (eds), Volume 3: Fluids, Chapter 17, Wiley, 2004.

18. Tezduyar TE. *Stabilized Finite Element Methods for Computation of Flows with Moving Boundaries and Interfaces*. Lecture Notes on Finite Element Simulation of Flow Problems (Basic-Advanced Course). Japan Society of Computational Engineering and Sciences: Tokyo, Japan, 2003.
19. Tezduyar TE, Behr M, Mittal S, Johnson AA. Computation of unsteady incompressible flows with the finite element methods—space–time formulations, iterative strategies and massively parallel implementations. *New Methods in Transient Analysis*, PVP-Vol. 246/AMD-Vol. 143. ASME: New York, 1992; 7–24.
20. Stein K, Tezduyar T, Benney R. Mesh moving techniques for fluid–structure interactions with large displacements. *Journal of Applied Mechanics* 2003; **70**:58–63.
21. Brown G, Haggard R, Benney R. Parachute retraction soft-landing systems using pneumatic muscle actuators. *Proceedings of AIAA 13th Guidance*, *Navigation and Control Conference*, Denver, CO, 2000.
22. Johari H, Stein K, Tezduyar T. Impulsively started flow about a rigid parachute canopy. *Journal of Aircraft* 2001; **38**:1102–1109.
23. Johari H, Stein K. Near wake of an impulsively started disk. *Physics of Fluids* 2002; **14**:3459–3474.

